Check for updates

Selective hydrogenation of furfural to furfuryl alcohol in water under mild conditions over a hydrotalcite-derived Pt-based catalyst

Ge Gao [a,b], Javier Remón [c,d], Zhicheng Jiang [a,b,*], Lu Yao [e], Changwei Hu [a,b,d,*]

[a] Department of Biomass Science and Engineering, Sichuan University, Chengdu 610065, PR China
[b] National Engineering Research Center of Clean Technology in Leather Industry, Sichuan University, Chengdu 610065, PR China
[c] Instituto de Carboquímica, CSIC, Zaragoza 50018, Spain
[d] Key Laboratory of Green Chemistry and Technology, Ministry of Education, College of Chemistry, Sichuan University, Chengdu 610064, PR China
[e] College of Architecture and Environment, Sichuan University, Chengdu 610065, PR China

ABSTRACT

The production of furfuryl alcohol (FFA) from biomass-derived furfural (FF) via selective hydrogenation is challenging due to the diverse unsaturated groups. Herein, a novel hydrotalcite-derived Pt-based catalyst was synthesized to catalyze the selective hydrogenation of FF to FFA in water. Within 2 h at 303 K and 1.5 MPa H_2, 99.9% conversion of FF with > 99% selectivity to FFA was obtained while the TOF being 204.6 h^{-1} and the E_a being 12.8 $kJmol^{-1}$. These results were accounted for by the 2D layered double hydroxides structure of hydrotalcite, which contributed to the high dispersion and effective reduction of Pt species, and the selective adsorption of the aldehyde group of FF on the catalyst, combined with the rapid desorption of the FFA produced. This guaranteed selective and stable hydrogenation over time, with up to four cycles ensured.

1. Introduction

Replacing petroleum-based chemicals for their renewable counterparts produced from biomass is not only a sustainable and green way to mitigate the over-reliance on fossil resources, but also contributory to palliate environmental issues [1–8]. Lignocellulose-derived furfural (FF) is one of the most versatile platform chemicals produced from biomass. It is widely used as the intermediate to furnish a wide range of products for the energy sector and the chemical and pharmaceutical industries [9–16]. Due to diverse unsaturated groups in the molecule, hydrogenation has been the dominant upgrading procedure to transform FF into different high-valued chemicals [17–22]. Among these, furfuryl alcohol (FFA) is considered a renewable-based, key chemical intermediate. About 65~70% of the global FF is currently converted to FFA [23,24], industrially used to manufacture pharmaceuticals such as lysine, ranitidine, farm chemicals, and various industrial products, such as plasticizers and resins [24,25].

The major problem to accomplish the hydrogenation of FF to FFA industrially is the development of side reactions, which decrease the selectivity toward FFA. For example, the hydrogenation of the furan ring into a tetrahydrofuran ring easily occurs. Besides, the hydrogenolysis of the hydroxyl or furan ring groups to form other by-products is also

plausible (Scheme 1). These latter include tetrahydrofurfural (THFF), tetrahydrofurfuryl alcohol (THFA), 2-methylfuran (2-MF), and 2-methyltetrahydrofuran (2-MTHF), attenuating the selectivity to FFA [18, 26–30]. Therefore, it is paramount to control the hydrogenation route to produce FFA selectively. With this being achieved, further by-products separation is avoided, which increases the profitability of the process and helps a possible process scale-up to bring this route to an industrial scale. Using Cr-based catalysts for the selective C=O hydrogenation of FF to FFA has been considered a commercially feasible alternative in the last decades [20,21]. However, an elevated reaction temperature (>413 K) was usually required for such a transformation, which led to high energy consumption and promoted more side reactions in some cases, resulting in the formation of several by-products [31,32]. Furthermore, it is also essential to consider the inherent environmental drawbacks of using Cr-based catalysts. Remarkably, the disposal of Cr into wastewater and solid residues causes severe environmental pollution and is a potential human health threat.

Therefore, it is necessary to develop green and non-toxic catalysts to avoid the use of toxic Cr. With this in mind, several Cr-free, low-temperature catalytic systems have been developed for the FF hydrogenation to FFA using various alcohols as the reaction medium. For example, it has been reported that PtNi hollow nanoframes, $NiBi/Al_2O_3$ and
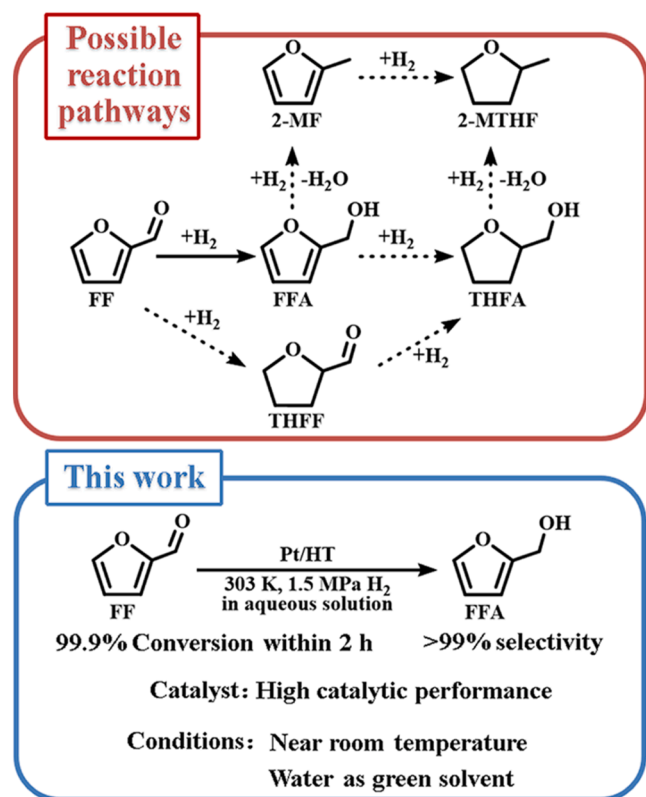
Scheme 1. The possible reaction pathways of FF hydrogenation and our work in selective carbonyl hydrogenation of FF to FFA.

$Pt_1Sn_{0.3}$ @HMSNs catalyzed the hydrogenation of FF to FFA using isopropanol as a solvent, and a > 97% selectivity was obtained at 373 K [33–35]. In another work, Pt/γ-Al_2O_3 catalyzed the FF hydrogenation, achieving about 80% yield of FFA with 99% selectivity at 323 K in methanol, and 45% FFA with 73% selectivity at 343 K when the process was conducted in ethanol [36]. These works pointed out that the reaction medium was important for catalytic performance. On the one side, polar alcohols (e.g., isopropanol, methanol, ethanol) were found to promote the adsorption of FF, as they help activate the hydrophilic C═O bonds of FF over the catalysts [22]. As a result, the catalytic hydrogenation efficiency toward FFA was significantly promoted. On the other, these alcohols caused the formation of other by-products, via either acetalization or esterification, which reduced the selectivity toward FFA [26,37,38].

Given these pros and cons, alternate reaction media should be sought, with water being an up-and-coming candidate. Using water facilitates solvent recycling and reduces safety risks for humans and the environment in comparison to alcohols. Besides, water decreased the activation energy barrier of the hydrogenation of the aldehyde group in FF through a water-mediated protonation process [39]. Despite it can promote the decarbonylation of FFA to 2-MF, thus decreasing FFA selectively [36], this can be avoided with a meticulous catalyst design and controlling the reaction conditions. Combining both strategies, high selectivity to FFA has been achieved in the aqueous phase. For instance, Pt/g-C_3N_4 could catalyze FF conversion to FFA with > 99% selectivity in water at 373 K with 75 h^{-1} of turn over frequency (TOF) [31]. After the reaction in an aqueous phase at 308 K for 12 h, 99% conversion of FF with 89% selectivity to FFA was obtained over a Pt/C catalyst [18]. In our previous work [40], a PtNi/SBA-15 catalyst was synthesized, and 84% of FF conversion with 1410 h^{-1} of TOF and 77% selectivity to FFA was achieved in water at 303 K. These publications are seen as the starting point for the selective hydrogenation of FF to FFA in water at mild conditions. However, there is still room for improvement, with

particular emphasis to be given to achieving high FFA selectivity using the lowest possible temperature.

As a novel contribution to this challenge, a highly-active catalyst (Pt/HT) comprising Pt nanoparticles loaded on the hydrotalcite-derived layered double oxides (LDO) support was prepared to hydrogenate FF into FFA. Hydrotalcite (HT, $Mg_6Al_2(OH)_{16}CO_3.4\ H_2O$) with a 2D layered double hydroxides (LDH) structure was chosen as the precursor of our hydrotalcite-derived Pt-based catalyst. LDH and its derived LDO improve the immobilization of Pt on the catalyst and also provide the material with high dispersion and excellent adsorption capabilities [41–43]. Other Pt-based catalysts supported on Mg and Al oxides were synthesized to gather the beneficial effect of the support. These include Pt/MgO, Pt/Al_2O_3 and Pt/MgO-Al_2O_3 (physical blending of the support). The structural features of these catalysts were thoroughly analyzed, and reliable comparisons have been established between their catalytic activity on the selective C═O hydrogenation of FF to obtain FFA under mild conditions in an aqueous phase. Finally, the stability of the Pt/HT catalyst was evaluated via recycling experiments of our green catalytic system, and a hydrogenation mechanism was proposed.

2. Experimental section

2.1. Materials

$H_2PtCl_6.6\ H_2O$ (99%), furfural (FF, 99%), furfuryl alcohol (98%), magnesium hydroxide ($Mg(OH)_2$, 95%), aluminum hydroxide ($Al(OH)_3$, AR), hydrotalcite ($Mg_6Al_2(OH)_{16}CO_3.4\ H_2O$, synthetic) were purchased from the commercial reagent companies. All chemicals were used as received without further purification.

2.2. Preparation of Pt-based catalysts

The 3 wt% Pt/HT catalyst was synthesized following the incipient wetness impregnation method. Before the impregnation, the HT was calcined at 773 K for 4 h (heating rate 2 K min^{-1}) to obtain the HT-calcined, used as the support. Then, 630 mg HT-calcined was mixed with 1 mL H_2PtCl_6 solution (0.1 mol L^{-1}), and the mixture was treated by ultrasonic vibration until well blended. After impregnation for 12 h, the mixture was dried directly in an oven at 353 K for 4 h. Afterward, the sample was calcined in air at 673 K for 1 h to obtain a catalyst precursor consisting of unreduced Pt species supported on HT-calcined (Pt/HT-unreduced). Prior to the experiments, the Pt/HT-unreduced was reduced by H_2 at 673 K for 1 h.

The 3 wt% Pt/Al_2O_3, 3 wt% Pt/MgO and 3 wt% Pt/MgO-Al_2O_3 catalysts were also prepared by the incipient wetness impregnation method. For the former, MgO and Al_2O_3 were respectively obtained from $Mg(OH)_2$ and $Al(OH)_3$ after 4 h calcination at 773 K. The process to obtain the MgO and Al_2O_3 supports from hydroxides was similar to that described for the HT-calcined. In the latter case, MgO and Al_2O_3 were physically mixed to obtain the MgO-Al_2O_3 support (the mole ratio of MgAl = 3, the same as in HT). Afterward, the preparation procedures for these three catalysts were the same as that described for the 3 wt% Pt/HT catalyst, i.e., metal-support impregnation, calcination and H_2 reduction. Due to the fact that Cl species have been found to have a promotional effect in the selective hydrogenation of α,β-unsaturated aldehydes [44], the catalysts have been prepared without washing to remove Cl^- in our experiments.

2.3. Solid catalysts characterizations

The nitrogen (N_2) physisorption measurements of the prepared catalysts were obtained by a Micromeritics ASAP 2460 analyzer. The structural properties were determined by the BET equation, following the BJH method. The X-ray diffraction (XRD) measurements of the prepared samples were carried out using a SHIMADZU XRD-6100 instrument. The X-ray photoelectron spectroscopy (XPS) analysis was

conducted on an Axis Ultra DLD (KRATOS) spectrometer. Before the above analyses, each solid sample was dried at 353 K, and then the dried solid samples were ground into 200 mesh powder.

The transmission electron microscope (TEM) images of synthesized catalysts were performed using a FEI Tecnai G2F20 (German). Before the TEM analysis, the solid samples were well dispersed in the water/ethanol solution by ultrasound. The above mixtures were loaded on copper grids and dried by infrared lamps.

The Pt loading of the prepared samples was analyzed by inductively coupled plasma emission spectrometry (ICP-AES) using a Germany Kleve Spectro. Before the ICP-AES analysis, each solid catalyst sample was dissolved in aqua regia at 423 K, and then a transparent solution without insolubilized solid matter was obtained and used for further quantification.

2.4. Hydrogenation experiments

For a typical hydrogenation experiment, FF (0.75 mmol), catalyst (50 mg) and H_2O (20 mL) were added into an autoclave reactor (50 mL). After replacing the air in the autoclave with H_2, the H_2 pressure in the autoclave stayed at 1.5 MPa. Afterward, the reaction system was heated to 303 K, and the speed of the magnetic stirrer was set at 600 rpm during the reaction process (2 h reaction time). Once the reaction terminated, the autoclave was cooled down to room temperature. Finally, the mixed products were poured out and separated by filtration.

2.4.1. Liquid products analysis

The liquid products were qualitatively determined by electrospray ionization mass spectrometry (ESI-MS) using a Shimadzu LCMS-IT-TOF, operated in a continuous mode. In addition, the liquid products were quantitatively determined by high-performance liquid chromatography (HPLC) using an Agilent 1260 Infinity apparatus, equipped with a Model HPX-87 P aminex column. According to the standard calibration curves, the components of liquid products were determined. The conversion of the substrate (C), yield (Y) and selectivity (S) of the products were calculated by Eqs. 1–3:

$$C = \frac{n_{initial} - n_{final}}{n_{initial}} \times 100\% \tag{1}$$

$$Y = \frac{n_{product}}{n_{initial}} \times 100\% \tag{2}$$

$$S = \frac{n_{product}}{n_{initial} - n_{final}} \times 100\% \tag{3}$$

In Eqs. (1–3), $n_{initial}$ is the moles of the added substrate, n_{final} accounts for the moles of the remained substrate in the post-treated liquid, and $n_{product}$ is the moles of each product in the post-treated liquid.

2.4.2. Calculation of TOF and TON

The metal dispersion of Pt (D_{Pt}), turn over number (TON) and turn over frequency (TOF) were calculated by Eqs. 4–6:

$$D_{Pt} = \frac{1.125}{average\ diameter\ of\ Pt} \times 100\% \tag{4}$$

$$TON = \frac{n_{initial} - n_{final}}{n_{Pt\ metal} \times D_{Pt}} \tag{5}$$

$$TOF(h^{-1}) = \frac{n_{initial} - n_{final}}{n_{Pt\ metal} \times D_{Pt} \times t} \tag{6}$$

In Eq. (4), the value 1.125 was employed by assuming spherical metal crystallites obtained by TEM analysis [40,45]. In Eqs. (5) and (6), t means the reaction time (10 min), and $n_{Pt\ metal}$ represents the moles of Pt metal on the supported catalysts determined by ICP-AES.

2.4.3. Calculation of the apparent activation energies

The FF hydrogenation to FFA in this study could be seen as the pseudo-first-order reaction due to the fact that H_2 is in significant excess. According to the literature [23,33], the chemical kinetics could be expressed by the empirical formulae shown in Eqs. (7) and (8),

$$C_0 - C_t = C_0 \left(1 - e^{-kt}\right) \tag{7}$$

$$X = \frac{C_0 - C_t}{C_0} \times 100\% \tag{8}$$

where C_0 accounts for the initial concentration of FF, C_t denotes the FF concentration at a particular reaction time (t) and k is the empirical kinetic constant (for the mass of catalyst used). The conversion of the reactant (X) can be obtained from Eq. (8).

The apparent activation energies (E_a) of the prepared catalysts were calculated by assuming that they followed the Arrhenius law using Eq. (9),

$$\ln k = -\frac{E_a}{RT} + \ln A \tag{9}$$

where T is reaction temperature (absolute temperature), k accounts for the kinetic reaction constant at this temperature and mass of catalyst used, A represents the pre-exponential factor, E_a denotes the apparent activation energy, with R being the universal gas constant.

2.5. Adsorption experiments

For a typical adsorption experiment, 50 mg catalyst was respectively mixed with two different solutions at room temperature (300 ± 3 K). One contains 5.0 mmol of FF in 20 mL H_2O, and the other comprises 5.0 mmol of FFA in 20 mL H_2O. After stirring for 30 min, filtration allowed the separation of the post-adsorbed catalyst from the reacted solution. Then, the solid samples were dried at 353 K and then analyzed by Fourier Transform Infrared (FT-IR) spectra. These solid sample analyses were conducted on a Nicolet Nexus 6700 spectrometer at room temperature with a spectral resolution of $2\ cm^{-1}$. Meanwhile, the reacted solutions after adsorption experiments were quantitatively determined by HPLC to analyze the residual FF/FFA. Additionally, the IR data of liquid FF/FFA and their water solutions were conducted at room temperature on a ReactIR IC10 system (Mettler Toledo, America) with a Mercury Cadmium Telluride detector.

3. Results and discussion

3.1. Catalysts textural characterizations

The textural properties of the supported Pt catalysts used in this work were determined by N_2 physisorption. The N_2 adsorption-desorption isotherms and pore diameter distributions obtained are shown in Fig. 1. In addition, Table 1 lists their corresponding textural properties. The hysteresis loop with H4 of type IV isotherm of Pt/Al2O3 reveals a dominant narrow slit-like porous structure. The pore diameter distributions of the Pt/Al2O3 catalysts present a narrow peak in the range of 0–10 nm, mainly ascribing to some mesopores present in its narrow slit-like porous structure [46]. On the contrary, the hysteresis loop for the Pt/MgO catalyst belongs to an H3 of type IV isotherm. This solid sample displays a bimodal distribution with pore diameters of 2–6 nm and 30–100 nm. Slit-shaped pores account for these mixed mesopores and macropores common in aggregated plate-like structures [46]. As described above, MgO and Al2O3 were mixed to make the MgO-Al2O3 support. The plate-like structure of MgO combined with the narrow slit-like mesopores present in Al2O3 led to a mixed H3-H4 of type IV isotherm hysteresis loop in the Pt/MgO-Al2O3 catalyst. As a result, the pore diameter distribution of the Pt/MgO-Al2O3 can be described by the additive combination of the MgO and Al2O3 structures. Although the
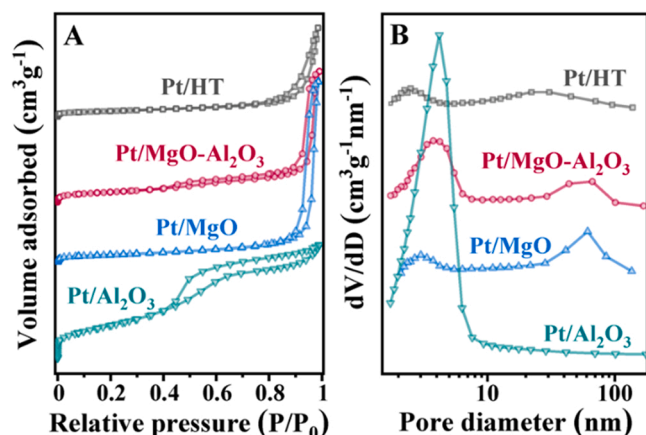
Fig. 1. The isotherms of N_2 physisorption (A) and the distributions of pore diameter (B) over the Pt-based catalysts.

Table 1
The BET results, metal diameters and metal loading of the prepared catalysts.

Catalyst	S_{BET}[a] (m^2 g^{-1})	Pore volume (cm^3 g^{-1})	d_{pore}[a] (nm)	d_{TEM}[b] (nm)	D_{Pt}[b] (%)	Actual Pt loading[c] (wt%)
3 wt% Pt/ HT	30.4	0.19	25.30	1.50	75.0	2.86
3 wt% Pt/ MgO-Al_2O_3	54.1	0.28	20.18	2.95	38.1	2.77
3 wt% Pt/ MgO	37.7	0.39	40.95	2.35	47.9	2.83
3 wt% Pt/ Al_2O_3	175.2	0.25	5.53	3.34	33.7	2.84

[a] S_{BET} denotes the BET surface area, d_{pore} means average pore diameter, obtained by N_2 physisorption.
[b] d_{TEM} represents the average diameter of Pt nanoparticles, D_{Pt} accounts for the metal dispersion of Pt, obtained from the TEM images.
[c] The results of actual Pt loading over the prepared catalysts were confirmed by ICP-AES.

hydrotalcite-derived LDO support also consisted of MgO and Al_2O_3, the textual structure of the hydrotalcite-derived LDO differs from that of the MgO-Al_2O_3 support. In this case, an H3 of type IV isotherm can be identified in the hysteresis loop of the Pt/HT catalyst, thus indicating that it has a similar structure to MgO with a plate-like morphology. It is worth mentioning that the two ranges of pore diameter distribution of the Pt/HT are wider and shifted toward the smaller pore diameter. This

helps increase the activity and deactivation resistance of the catalyst as the plate-like structures with slit-shaped pores of the hydrotalcite-derived LDO support benefit the immobilization and dispersion of active metals. In addition, it boosts the selective adsorption of reactants and rapid desorption of products [41,42].

The crystalline structures of the catalysts and their precursors were determined by XRD (Fig. 2A). The standard diffraction peaks of HT (PDF#41–1428) are clearly observed in the analysis of the commercial HT. After the calcination pre-treatment, two new peaks appeared, ascribing to the dehydration of HT to produce a new MgO-Al_2O_3 (mixed metal oxides) phase [47]. This new MgO-Al_2O_3 phase can be classified as MgAl-mixed oxides, which can easily recover the original LDH structure of HT in water [29,47,48]. Such a phenomenon can be observed in Fig. S1. Furthermore, no characteristic diffraction peaks of PtO_2 or Pt are observed in the XRD diffractograms of either the Pt/HT-unreduced or the Pt/HT catalyst. This confirms the high dispersion of Pt species on the hydrotalcite-derived LDO support. Fig. 2B shows the XRD diffractograms of the catalysts after H_2 reduction. The XRD diffractograms of Pt/Al_2O_3 presented the characteristic (2 0 7) and (1 1 14) planes attributed to Al_2O_3 (PDF#51–0769). Besides, the Al_2O_3 phase with low crystallinity was classified as an amorphous Al_2O_3 and γ-Al_2O_3 mixture, possibly composed of nano-size Al_2O_3 particles. The typical (1 1 1), (2 0 0), (2 2 0), (3 1 1) and (2 2 2) planes corresponding to MgO (PDF#45–0946) are identified in the XRD diffractograms of Pt/MgO. Additionally, the sharp diffraction peaks of MgO revealed the good crystallization of MgO phases in the Pt/MgO catalyst. The XRD diffractograms of Pt/MgO-Al_2O_3 includes the diffraction peaks of MgO planes and Al_2O_3 planes, revealing that both solid were physically well-mixed to produce MgO-Al_2O_3. On the contrary, there are only two peaks in the case of the Pt/HT catalyst, and these correspond to MgAl-mixed oxides rather than the typical peaks of MgO or Al_2O_3. From the enlarged XRD diffractograms of Pt in the inset of Fig. 2B, the diffraction peak of Pt (1 1 1) plane (PDF#04–0802) could only be detected on Pt/MgO, Pt/Al_2O_3 and Pt/MgO-Al_2O_3, indicating the successful immobilization of Pt particles on these supports and the smaller Pt particle size on the hydrotalcite-derived LDO support than others. The smaller Pt particles contributed to a high utilization rate of Pt metal. The result further proved that the HT-derived support provided the highest metal dispersion performance over the supports considered.

The morphology of the catalysts examined by TEM is presented in Fig. 3, and the average diameters of Pt particles on the different prepared catalysts are summarized in Table 1. On the one side, the structure of Pt/Al_2O_3 showed a lumpy morphology (500–1000 nm in diameter) with obvious mesoporosity. On the other, Pt/MgO consisted of small layers (about 50 nm) conforming to a multilayer structure. This was inherited by the Pt/MgO-Al_2O_3 catalyst, which consists of a mixture of
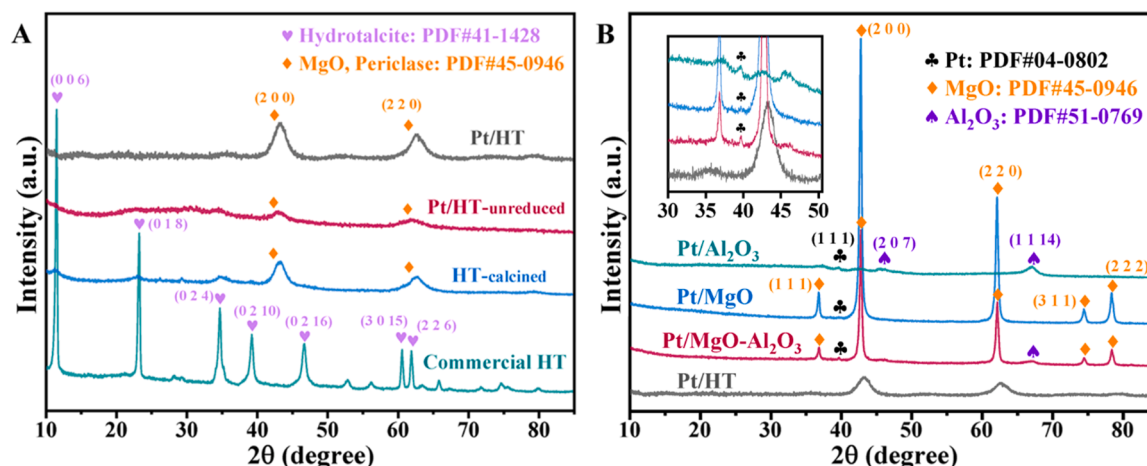

Fig. 2. XRD data as diffractograms of Pt/HT in different preparation steps (A) and these freshly prepared catalysts after H_2 reduction (B).
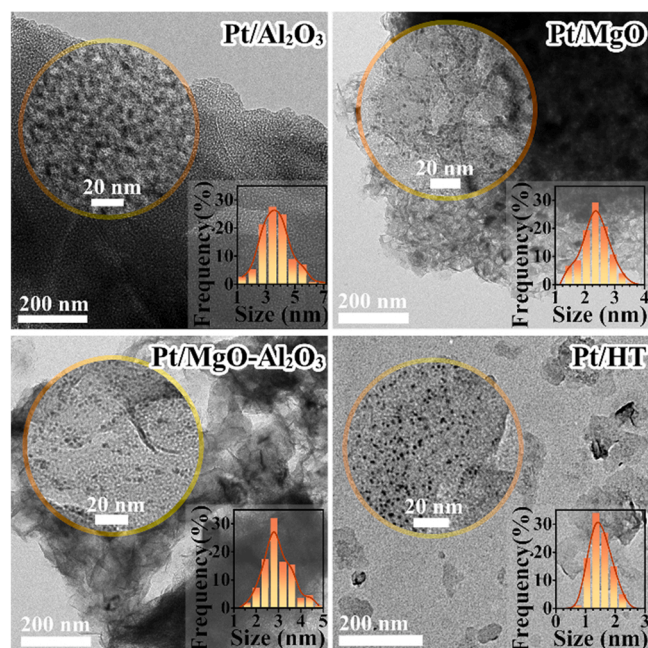
Fig. 3. TEM images and Pt nanoparticles size distributions of the synthesized catalysts.

Fig. 4. XPS of these prepared catalysts in Pt 4 f spectra. (The red, blue and cyan lines represent Pt^0, Pt^{2+} and Pt^{4+} signals, respectively. The gray dotted lines represent the Al-subtracted Pt 4 f spectra. The purple lines account for the expected binding energies of standard Pt metal.).

both morphologies (multilayer and lumpy morphologies). The mean sizes of Pt nanoparticles on these catalysts are 3.34, 2.35 and 2.95 nm, respectively. Noticeably, the Pt/HT catalyst shows a flower-like morphology composed of individual layers. The mean size (1.50 nm) of the Pt nanoparticles on the Pt/HT catalyst is significantly smaller than that of the others. Besides, the diameters of the Pt particles are intensively distributed in the range of 1–2 nm, indicating that the 2D lamellar structure could facilitate the formation of a catalyst containing Pt nanoparticles and smaller in size and better dispersed onto the support. Despite the surface area of Pt/HT was relatively low compared with other materials (Table 1), the anion exchanges between the unique support and the $PtCl_6^{2-}$ precursor facilitated the uniform dispersion of Pt on the catalyst. Consequently, these smaller, well-dispersed Pt particles could increase atom utilization and enlarge the active catalytic surface of the catalyst.

The valence states of the metal species in the catalysts were determined by XPS (Fig. 4 and Fig. S2). For the prepared Pt-based catalysts, the Pt 4d feature was weaker than Pt 4 f, which overlapped with the Mg KLL feature. Due to the high Mg content of hydrotalcite-derived LDO support or MgO, the serious interference of Mg KLL prevented the analysis of the Pt 4d feature. Therefore, the Pt 4 f feature with Al 2p interference was used for the analysis of Pt valence states in this work. Before analyzing the Pt spectra, the overlapping Al 2p peak at 74.3 eV was subtracted [49]. This was intended to avoid interference, as the Pt 4 f spectra exhibited two peaks at 71.0 and 74.4 eV, attributing to 4 $f_{7/2}$ and 4 $f_{5/2}$ (resulting from the spin-orbit splitting). The Pt 4 f spectra were successfully fitted to Pt^0, Pt^{2+} and Pt^{4+} signals, which allowed us to calculate the relative contents of Pt species. From these calculations, the relative contents of Pt^0 are 54.9% in Pt/Al$_2$O$_3$, 65.2% in Pt/MgO, 65.5% in Pt/MgO-Al$_2$O$_3$, and 72.5% in Pt/HT. These results indicate that Pt^0 was the main species in these catalysts. This accounts for an efficient reduction of H_2PtCl_6 during the catalyst preparation. The different dispersion behavior and Pt-support interactions in the catalysts led to different distributions of Pt species. In particular, the Pt/HT catalyst exhibits the highest Pt^0 relative content. This proves evidence for the very high reducibility of Pt in the Pt/HT catalyst, which can also explain the excellent dispersion of this metal onto the support. These phenomena endorse the catalyst with excellent catalytic activity. For hydrogenation reactions, small Pt particles with a high proportion of complete reduced species, i.e., Pt^0, exert a significant catalytic effect [36,42,50].
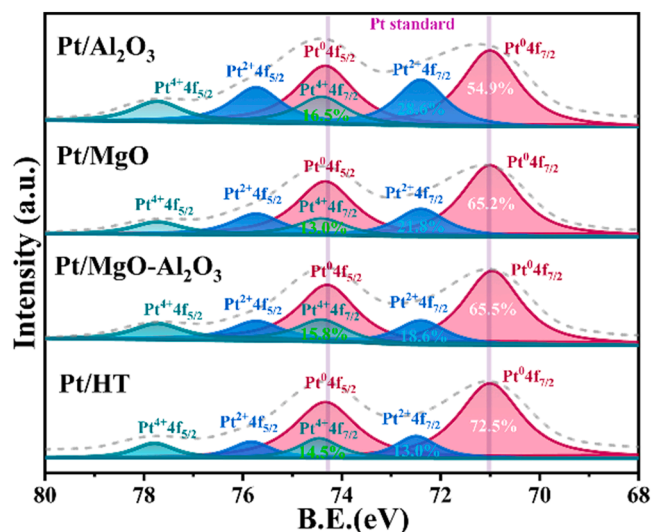
3.2. Catalytic hydrogenation of FF

The catalytic hydrogenation of FF to FFA over different catalysts was compared in water at nearly room temperature (303 K). This system was chosen to increase the selectivity of FFA. On the one side, water was used as a solvent, as it facilitates the hydrogen exchange processes between H$_2$ and reactants, thus boosting the hydrogenation of FF [39]. On the other, the process was conducted at a low temperature to minimize the extension of secondary reactions.

Fig. 5 A and B shows the catalytic activity of the prepared catalysts. Regarding the support effect, the experimental results reveal that it exerts a significant influence on the conversion of FF and the selectivity to FFA. When the process is conducted in the presence of the Pt/HT or Pt/MgO catalysts, much higher conversions are obtained than with Pt/MgO-Al$_2$O$_3$ or Pt/Al$_2$O$_3$. In particular, the conversion of FF over Pt/HT is almost complete (96.9%) within 1 h of reaction, displaying a plateau with further increasing the reaction time. In comparison, the conversions of FF over Pt/MgO-Al$_2$O$_3$ and Pt/Al$_2$O$_3$ at 1 h treatment were only 57.2% and 39.9%, respectively. FFA was the main reaction product in all cases, though small amounts of oligomers and other byproducts were also generated in the initial period of the reaction (Fig. S3). Interestingly, as the reaction progresses, the selectivity to FFA increases, with such a rise depending on the catalyst. For example, it is as high as 99% for the Pt/HT, Pt/MgO-Al$_2$O$_3$ and Pt/MgO catalysts, while only 88.6% over Pt/Al$_2$O$_3$. These data highlight that Pt/HT exhibited the most outstanding hydrogenation performance among these catalysts, with 99.9% FF conversion and > 99% FFA selectivity at 303 K within 2 h. These results are breakthroughs for FFA production. The processing conditions used help diminish the energy input and facilitate the separation of the products (high conversion and selectivity), thus improving the profitability of this transformation.

As shown in Fig. 5D and Table 2, an increase in the reaction temperature from 303 to 323 K significantly accelerates the hydrogenation of FF to FFA. According to Fig. 5 C and the previous reports, since this could be considered a pseudo-first-order reaction [23,33], the apparent activation energies (E_a) of these catalysts have been calculated via the numerical regression and Arrhenius law. Among the different catalysts, the reference Pt/Al$_2$O$_3$ catalyst has the highest E_a (22.6 kJ mol^{-1}), whereas the optimal Pt/HT catalyst displays the lowest E_a
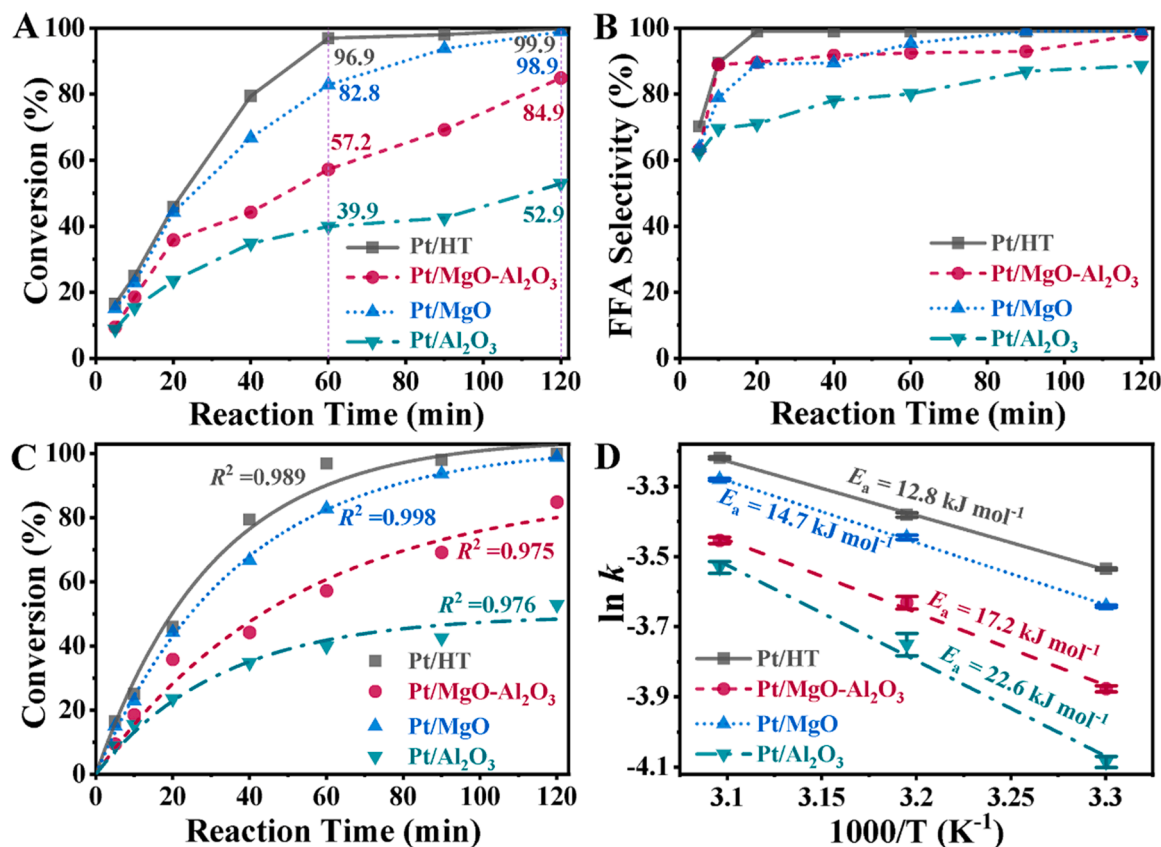
Fig. 5. Catalytic hydrogenation of FF over these prepared catalysts. (A: FF conversion-reaction time data, B: FFA selectivity-reaction time data, C: the curves of chemical kinetics, D: the Arrhenius regressions.) Reaction conditions: 0.75 mmol FF, 50 mg catalyst, 20 mL of H_2O, 1.5 MPa H_2.

Table 2
The hydrogenation of FF over these catalysts at different temperatures for 10 min.

Catalysts	Temp. (K)	Conv. (%)	k (min^{-1})	TOF (h^{-1})	$E_{a\ (kJ\ mol^{-1})}$
Pt/HT	303	25.0	0.0288	204.6	12.8
	313	28.5	0.0336	233.3	
	323	32.6	0.0395	266.8	
Pt/MgO-Al$_2$O$_3$	303	18.5	0.0205	307.8	17.2
	313	23.0	0.0261	382.6	
	323	26.8	0.0312	445.8	
Pt/MgO	303	22.8	0.0259	295.3	14.7
	313	27.0	0.0315	349.7	
	323	31.0	0.0371	401.5	
Pt/Al$_2$O$_3$	303	15.3	0.0166	280.7	22.6
	313	17.8	0.0232	326.5	
	323	20.2	0.0289	370.6	

Temp. means reaction temperature. Conv. denotes the conversion of FF. Reaction conditions: 0.75 mmol FF, 50 mg catalyst, 20 mL of H_2O, 1.5 MPa H_2. k is the reaction rate (kinetic) constant for 50 mg catalyst.

(12.8 kJ mol^{-1}). Besides, the TOF on Pt/HT was as high as 204.6 h^{-1} at 303 K. These results indicate that the Pt/HT catalyst was the most active and highlight the significant effect of the support. The hydrotalcite-derived LDO support was essential to effectively activate FF, which was further hydrogenated to FFA under mild conditions, with these transformations taking place substantially and selectively.

Apart from FF, different α,β-unsaturated aldehydes, such as 5-hydroxymethylfurfural (HMF), 5-methylfurfural (5-MF), are widely generated in the C═O hydrogenation processes. Therefore, the capability of our Pt/HT catalyst to hydrogenate various biomass-derived furfural-like chemicals was also investigated. As shown in Table 3, Pt/HT displayed both 99.9% conversions of FF and HMF, with the

Table 3
The hydrogenations of various furfural-derived aldehydes over Pt/HT.

Substrate	Product	Time	Conv. (%)	Selec. (%)
FF	FFA	2 h	99.9	> 99
5-MF	5-MFA	2 h	50.1	> 99
5-MF	5-MFA	8 h	99.0	> 99
HMF	DHMF	2 h	99.9	94.5

Conv. and Selec. respectively represent the conversion of the substrate and the selectivity to a product. Reaction conditions: 0.75 mmol substrate, 50 mg Pt/HT, 20 mL of H_2O, 303 K, 1.5 MPa H_2.

selectivity toward FFA and 2,5-dihydroxymethylfuran (DHMF) being > 99% and 94.5%, respectively, within 2 h. Although the hydrogenation rate of 5-MF was relatively slower, prolonging the reaction time could promote the complete conversion of 5-MF into 5-methyl-2-furanmethanol (5-MFA) with > 99% selectivity. Our experimental results demonstrate that the Pt/HT catalyst selectively hydrogenates C═O bonds for α,β-unsaturated aldehydes preserving the furan ring structure. These results highlight the excellent capabilities of our Pt/HT catalyst for the selective hydrogenation of biomass-derived species at low temperatures and using water as a reaction medium. We believe this is a step forward in this field, which can pave the way for an efficient chemical upgrading of different biomass-derived platform molecules.

3.3. Selective C═O adsorption of FF and hydrogenation pathways

As the adsorption-desorption step is critical when designing effective and selective catalysts for a process [30], the adsorptions of FF (reactant) and FFA (product) on these catalysts were calculated and compared. As shown in Fig. 6A, the adsorption of FF on these catalysts is stronger than that of FFA. The Pt/HT displays the highest adsorption
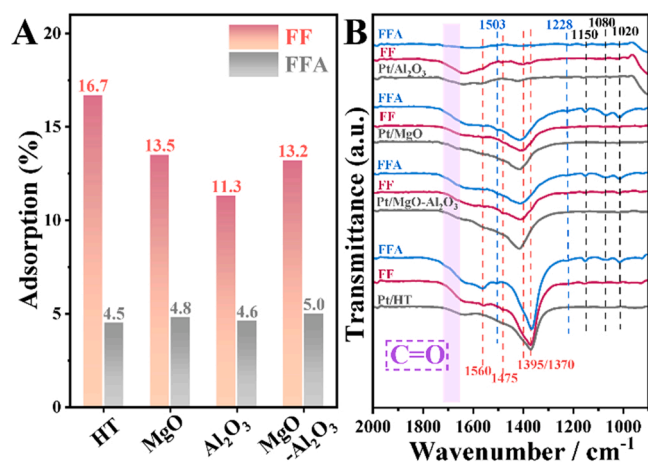
Fig. 6. (A) The results of FF or FFA adsorption over these Pt-based catalysts with different supports and (B) the FT-IR spectrums of these catalysts and post-adsorbed samples (black: fresh catalyst, red: FF adsorbed sample, blue: FFA adsorbed sample).

Scheme 2. Schematic diagram for the catalytic mechanism of FF selective hydrogenation.

rate for FF and the lowest adsorption rate for FFA among the four catalysts. The preferential adsorption of the C=O bond on Pt/HT might be responsible for the different adsorption behaviors of FF and FFA, consequently boosting the selective hydrogenation of the aldehyde group of FF. Meanwhile, the weak adsorption of FFA also promotes its rapid desorption from the catalyst. This avoids over hydrogenation and exposes more active sites of catalysts for continuous FF hydrogenation, which in combination leads to an increase in conversion and selectivity. FT-IR was also employed to analyze these post-adsorbed catalysts (Fig. 6B and Fig. S4). Compared with the standard FF/FFA data, the peaks at 1560, 1475, 1395 and 1370 cm^{-1} revealed the successful adsorption of FF on the catalysts, but the substantial interference of the Mg-O band affected the FTIR spectra of Pt/HT, Pt/MgO and Pt/MgO-Al$_2$O$_3$. In addition, the broad band (1550–1700 cm^{-1} range) should be characteristic of the H–O bending mode owing to the deformation vibration of chemisorbed water. Although the strong adsorptions of FF can be determined by the HPLC data, the band of ν(C=O), which should appear at about 1650–1720 cm^{-1}, was invisible on the FTIR data of FF-adsorbed samples. This is possibly due to the strong interaction between Pt(5d) and C=O(2π*), the C=O stretching band was weakened. The result indicated the existence of the η^2(C, O)-aldehyde conformation on these Pt-based catalysts rather than an η^1(O)-aldehyde conformation. An intermediate species might be formed during the FF adsorption on the Pt-based catalysts, promoting selective C=O hydrogenation [39]. For the FFA-adsorbed samples, the weak peaks at 1503 and 1228 cm^{-1} and sharp peaks at 1150, 1080 and 1020 cm^{-1} also revealed the successful adsorption of FFA. The peaks at 1150 and 1080 cm^{-1}, respectively assigned to the C-O-C band and C-O linearly adsorbed with O terminal band [43], are observed on the Pt/MgO catalyst after the FFA adsorption, which could reveal the stronger chemisorption and the η^1(O)-hydroxyl conformation on Pt/MgO. Given these data, the stronger adsorption interaction between FFA and Pt/MgO could restrain the desorption of FFA. This results in a slower FF hydrogenation rate on the Pt/MgO than that on the Pt/HT catalyst.

According to the above adsorption experiments and catalytic activities in FF hydrogenation, the hydrogenation pathways from FF to FFA over the Pt/HT catalyst could be divided into four main steps shown in Scheme 2. A gaseous H$_2$ is adsorbed first on Pt surfaces, and dissociated into activated hydrogen atoms before the catalytic hydrogenation. The d-orbitals of Pt donate d-electrons to the σ antibonding orbital of hydrogen, which facilitates the cleavage of the H–H bond [33]. The high dispersion combined with the small size of Pt particles promotes this process. Then, the aldehyde group in FF is adsorbed on the Pt/HT catalyst. In reaching this point, the interaction between Pt(5d) and C=O
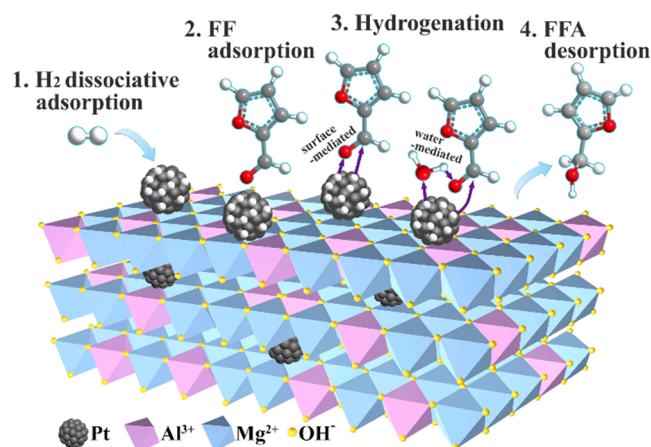
(2π*) increases the probability of C=O bond activation [30]. At the same time, the interaction between Pt and C=C is weakened and the activity of the C=C bond decreases by increasing repulsive four-electron interaction [51]. Meanwhile, abundant hydroxyls on the LDH structure inhibit the interaction with the C=C bond by electrostatic repulsion, whilst the hydrophilicity of the LDH sites benefits the orientation of the hydrophilic C=O moiety [41]. Subsequently, the adsorbed FF is converted to FFA by the pre-activated hydrogen. In addition to this surface-mediated hydrogenation pathway, water-mediated hydrogenation occurs concurrently. For this, water, as a solvated proton (H$_3$O$^+$), reduces the activation barrier and promotes the hydrogenation of FF to FFA [39]. Finally, the generated FFA is desorbed from the catalyst surface. This takes place efficiently due to the weak adsorption of FFA on the catalyst, avoiding over-hydrogenation, and therefore, leaving more active sites on the Pt/HT catalyst exposed for further hydrogenation.

3.4. Scale-up and stability experiments for the FF hydrogenation over Pt/HT

Different experiments were conducted to address the commercial application of this catalytic system (active catalyst, water as a reaction medium at low temperature) to transform FF into FFA (Table 4) selectively. These cover the use of high substrate concentrations and the possibility of recycling the catalyst. When the concentration of FF increases from 0.75 to 5.0 mmol (the ratio of substrate to active metal changed from 102 to 682 mol$_{FF}$ mol^{-1}$_{Pt}$), although a noticeable decrease in the FF conversion is observed, the selectivity to FFA remains high (>99%). Increasing the amount of catalyst from 50 to 200 mg and prolonging the reaction time from 2 to 8 h, 99.9% conversion of FF and > 99% selectivity to FFA are obtained at 303 K. Then recycling experiments were accomplished to analyze the stability and reusability of the Pt/HT catalyst. The objective was to determine whether or not this

Table 4
The scale-up and stability experiments for the FF hydrogenation over Pt/HT.[a]

Substrate (mmol)	Mass of Catalysts	Conversion (%)	TON	FFA Selectivity (%)
0.75	50 mg	99.9[b]	136.3	> 99
5.0	50 mg	37.4	340.1	> 99
5.0	200 mg (1st)	99.9	227.1	> 99
5.0	200 mg (2nd)	99.9	227.1	98.3
5.0	200 mg (3rd)	99.2	225.5	96.0
5.0	200 mg (4th)	97.8	222.4	96.3

[a] Reaction conditions: furfural as substrate, 20 mL H$_2$O, 1.5 MPa H$_2$, 303 K, Reaction time: 8 h
[b] The reaction time was 2 h in this entry.

process could be scaled-up and brought to a commercial scale. After each hydrogenation reaction, the Pt/HT catalyst was readily separated from the reaction mixture by filtration. It was then dried and used for the subsequent hydrogenation reaction without extra H_2 reduction. These tests show a slight decline in the conversion of FF (99.9% ~97.8%) and the selectivity to FFA (>99% ~96.3%) after four successive cycles. The characterization of the spent Pt/HT catalyst showed that it still maintained the well-reserved layer structure, with the Pt nanoparticles being well-dispersed and the Pt content being well-preserved over the cycles (Fig. S5 and Table S1). Its outstanding stability and reusability make it an excellent catalytic material for the industrial hydrogenation of furans.

4. Conclusions

In this work, a novel catalyst consisting of Pt nanoparticles supported on hydrotalcite (Pt/HT) was synthesized and thoroughly characterized. Its catalytic activity was tested in the water phase hydrogenation of furfural (FF) to furfuryl alcohol (FFA) at a low temperature. Within 2 h at 303 K and 1.5 MPa H_2 pressure, 99.9% conversion of FF with > 99% selectivity to FFA was obtained while the TOF being as high as 204.6 h^{-1} and the E_a as low as 12.8 $kJmol^{-1}$. To gain more insights into the effect of the support, Pt nanoparticles were also supported on Al_2O_3, MgO and Al_2O_3-MgO. Experimental results demonstrated that the outstanding catalytic performance of Pt/HT was attributed to its unique LDH structure. This provided the catalyst with an excellent Pt dispersion and favored the reduction of the Pt precursor, which increased the proportion of Pt^0 species. Both parameters not only favored the C=O adsorption and activation of FF but also boosted the activation and adsorption of H_2 onto the catalyst. The different adsorption-desorption capabilities of FF and FFA on the catalyst were paramount to ensure high activity and selectivity. In particular, the weak adsorption of FFA promoted its rapid desorption, thus exposing more active sites in the catalyst for continuous FF hydrogenation. As regards the possible industrial applicability of this catalyst, excellent stability (>97.8% FF conversion and >96.3% FFA selectivity during four recycling tests) was attained over four consecutive tests, with the catalyst being easily recoverable from reaction liquid. Furthermore, our Pt/HT catalyst also showed excellent capabilities for hydrogenating other α,β-unsaturated aldehydes, such as 5-MF and HMF. Given the exceptional catalytic capabilities in terms of conversion, selectivity and stability of our catalyst, coupled with its tremendous versatility to hydrogenate different biomass-derived furan compounds and the green processing conditions used, this work is a step-change to furnish a wide range of reaction products from biomass.

CRediT authorship contribution statement

Ge Gao: Investigation, Writing – original draft, Data curation. **Javier Remón:** Investigation, Methodology, Writing – review & editing. **Zhicheng Jiang:** Investigation, Funding acquisition, Writing – review & editing. **Lu Yao:** Investigation, Writing – review & editing. **Changwei Hu:** Funding acquisition, Supervision, Resources, Methodology, Writing – review & editing.

Declaration of Competing Interest

The authors declare that they have no known competing financial interests or personal relationships that could have appeared to influence the work reported in this paper.

Acknowledgment

Appendix A. Supporting information

Supplementary data associated with this article can be found in the online version at doi:10.1016/j.apcatb.2022.121260.

References

[1] P. Sudarsanam, E. Peeters, E.V. Makshina, V.I. Parvulescu, B.F. Sels, Advances in porous and nanoscale catalysts for viable biomass conversion, Chem. Soc. Rev. 48 (2019) 2366–2421, https://doi.org/10.1039/c8cs00452h.

[2] L.T. Mika, E. Csefalvay, A. Nemeth, Catalytic conversion of carbohydrates to initial platform chemicals: chemistry and sustainability, Chem. Rev. 118 (2018) 505–613, https://doi.org/10.1021/acs.chemrev.7b00395.

[3] H. Luo, J. Barrio, N. Sunny, A. Li, L. Steier, N. Shah, I.E.L. Stephens, M.M. Titirici, Progress and perspectives in photo- and electrochemical-oxidation of biomass for sustainable chemicals and hydrogen production, Adv. Energy Mater. 11 (2021), 2101180, https://doi.org/10.1002/aenm.202101180.

[4] G. Jyoti, P. Konstantinos, K. Elena Yu, L. Yi, V.K. Ivan, L. Jingjing, CaO catalyst for multi-route conversion of oakwood biomass to value-added chemicals and fuel precursors in fast pyrolysis, Appl. Catal. B: Environ. (2021), https://doi.org/10.1016/j.apcatb.2020.119858.

[5] L. Dai, Y. Wang, Y. Liu, C. He, R. Ruan, Z. Yu, L. Jiang, Z. Zeng, Q. Wu, A review on selective production of value-added chemicals via catalytic pyrolysis of lignocellulosic biomass, Sci. Total Environ. 749 (2020), 142386, https://doi.org/10.1016/j.scitotenv.2020.142386.

[6] X. Chen, S. Song, H. Li, G. Gozaydin, N. Yan, Expanding the boundary of biorefinery: organonitrogen chemicals from biomass, Acc. Chem. Res. 54 (2021) 1711–1722, https://doi.org/10.1021/acs.accounts.0c00842.

[7] X. Liu, F.P. Bouxin, J. Fan, V.L. Budarin, C. Hu, J.H. Clark, Recent advances in the catalytic depolymerization of lignin towards phenolic chemicals: a review, ChemSusChem 13 (2020) 4296–4317, https://doi.org/10.1002/cssc.202001213.

[8] R. Xu, K. Liu, H. Du, H. Liu, X. Cao, X. Zhao, G. Qu, X. Li, B. Li, C. Si, Falling leaves return to their roots: a review on the preparation of gamma-valerolactone from lignocellulose and its application in the conversion of lignocellulose, ChemSusChem 13 (2020) 6461–6476, https://doi.org/10.1002/cssc.202002008.

[9] Y.P. Luo, Z. Li, X.L. Li, X.F. Liu, J.J. Fan, J.H. Clark, C.W. Hu, The production of furfural directly from hemicellulose in lignocellulosic biomass: a review, Catal. Today 319 (2019) 14–24, https://doi.org/10.1016/j.cattod.2018.06.042.

[10] S. Chen, R. Wojcieszak, F. Dumeignil, E. Marceau, S. Royer, How catalysts and experimental conditions determine the selective hydroconversion of furfural and 5-hydroxymethylfurfural, Chem. Rev. 118 (2018) 11023–11117, https://doi.org/10.1021/acs.chemrev.8b00134.

[11] R. Mariscal, P. Maireles-Torres, M. Ojeda, I. Sádaba, M.L.ópez Granados, Furfural: a renewable and versatile platform molecule for the synthesis of chemicals and fuels, Energy Environ. Sci. 9 (2016) 1144–1189, https://doi.org/10.1039/c5ee02666k.

[12] C. Xu, E. Paone, D. Rodriguez-Padron, R. Luque, F. Mauriello, Recent catalytic routes for the preparation and the upgrading of biomass derived furfural and 5-hydroxymethylfurfural, Chem. Soc. Rev. 49 (2020) 4273–4306, https://doi.org/10.1039/d0cs00041h.

[13] H. Zhang, M. Jiang, Y. Wu, L. Li, Z. Wang, R. Wang, G. Zhou, Development of completely furfural-based renewable polyesters with controllable properties, Green. Chem. 23 (2021) 2437–2448, https://doi.org/10.1039/d1gc00221j.

[14] R. Karinen, K. Vilonen, M. Niemela, Biorefining: heterogeneously catalyzed reactions of carbohydrates for the production of furfural and hydroxymethylfurfural, ChemSusChem 4 (2011) 1002–1016, https://doi.org/10.1002/cssc.201000375.

[15] K. Yan, G. Wu, T. Lafleur, C. Jarvis, Production, properties and catalytic hydrogenation of furfural to fuel additives and value-added chemicals, Renew. Sust. Energ. Rev. 38 (2014) 663–676, https://doi.org/10.1016/j.rser.2014.07.003.

[16] C. Espro, E. Paone, F. Mauriello, R. Gotti, E. Uliassi, M.L. Bolognesi, D. Rodriguez-Padron, R. Luque, Sustainable production of pharmaceutical, nutraceutical and bioactive compounds from biomass and waste, Chem. Soc. Rev. 50 (2021) 11191–11207, https://doi.org/10.1039/d1cs00524c.

[17] K. Fulajtárova, T. Soták, M. Hronec, I. Vávra, E. Dobročka, M. Omastová, Aqueous phase hydrogenation of furfural to furfuryl alcohol over Pd–Cu catalysts, Appl. Catal. A: Gen. 502 (2015) 78–85, https://doi.org/10.1016/j.apcata.2015.05.031.

[18] J. Wu, X. Zhang, Q. Chen, L. Chen, Q. Liu, C. Wang, L. Ma, One-pot hydrogenation of furfural into tetrahydrofurfuryl alcohol under ambient conditions over PtNi alloy catalyst, Energy Fuels 34 (2019) 2178–2184, https://doi.org/10.1021/acs.energyfuels.9b02811.

[19] Y. Fan, S. Li, Y. Wang, C. Zhuang, X. Liu, G. Zhu, X. Zou, Tuning the synthesis of polymetallic-doped ZIF derived materials for efficient hydrogenation of furfural to furfuryl alcohol, Nanoscale 12 (2020) 18296–18304, https://doi.org/10.1039/d0nr04098c.

[20] R.V. Sharma, U. Das, R. Sammynaiken, A.K. Dalai, Liquid phase chemo-selective catalytic hydrogenation of furfural to furfuryl alcohol, Appl. Catal. A: Gen. 454 (2013) 127–136, https://doi.org/10.1016/j.apcata.2012.12.010.

[21] R. Rao, A. Dandekar, R.T.K. Baker, M.A. Vannice, Properties of copper chromite catalysts in hydrogenation reactions, J. Catal. 171 (1997) 406–419, https://doi.org/10.1006/jcat.1997.1832.

[22] X. Gao, S. Tian, Y. Jin, X. Wan, C. Zhou, R. Chen, Y. Dai, Y. Yang, Bimetallic PtFe-catalyzed selective hydrogenation of furfural to furfuryl alcohol: solvent effect of isopropanol and hydrogen activation, ACS Sustain. Chem. Eng. 8 (2020) 12722–12730, https://doi.org/10.1021/acssuschemeng.0c04891.

[23] Y. Wang, T. Gao, Y. Lu, Y. Wang, Q. Cao, W. Fang, Efficient hydrogenation of furfural to furfuryl alcohol by magnetically recoverable RuCo bimetallic catalyst, Green. Energy Environ. (2020), https://doi.org/10.1016/j.gee.2020.09.014.

[24] B. Roman, G. Grzegorz, Furan platform chemicals beyond fuels and plastics, Green. Chem. (2021), https://doi.org/10.1039/d1gc02402g.

[25] A. Gandini, Furans as offspring of sugars and polysaccharides and progenitors of a family of remarkable polymers: a review of recent progress, Polym. Chem. 1 (2010) 245–251, https://doi.org/10.1039/b9py00233b.

[26] M.J. Islam, M. Granollers Mesa, A. Osatiashtiani, M.J. Taylor, J.C. Manayil, C.M. A. Parlett, M.A. Isaacs, G. Kyriakou, The effect of metal precursor on copper phase dispersion and nanoparticle formation for the catalytic transformations of furfural, Appl. Catal. B: Environ. 273 (2020), 119062, https://doi.org/10.1016/j.apcatb.2020.119062.

[27] M.J. Taylor, S.K. Beaumont, M.J. Islam, S. Tsatsos, C.A.M. Parlett, M.A. Issacs, G. Kyriakou, Atom efficient PtCu bimetallic catalysts and ultra dilute alloys for the selective hydrogenation of furfural, Appl. Catal. B: Environ. 284 (2021), 119737, https://doi.org/10.1016/j.apcatb.2020.119737.

[28] Z. Lin, W. Wan, S. Yao, J.G. Chen, Cobalt-modified molybdenum carbide as a selective catalyst for hydrodeoxygenation of furfural, Appl. Catal. B: Environ. 233 (2018) 160–166, https://doi.org/10.1016/j.apcatb.2018.03.113.

[29] Y.D. Yang, Y.Y. Wang, S.P. Li, X.J. Shen, B.F. Chen, H.Z. Liu, B.X. Han, Selective hydrogenation of aromatic furfurals into aliphatic tetrahydrofurfural derivatives, Green. Chem. 22 (2020) 4937–4942, https://doi.org/10.1039/d0gc01587c.

[30] M. Luneau, J.S. Lim, D.A. Patel, E.C.H. Sykes, C.M. Friend, P. Sautet, Guidelines to achieving high selectivity for the hydrogenation of alpha,beta-unsaturated aldehydes with bimetallic and dilute alloy catalysts: a review, Chem. Rev. 120 (2020) 12834–12872, https://doi.org/10.1021/acs.chemrev.0c00582.

[31] X. Chen, L. Zhang, B. Zhang, X. Guo, X. Mu, Highly selective hydrogenation of furfural to furfuryl alcohol over Pt nanoparticles supported on g-C3N4 nanosheets catalysts in water, Sci. Rep. 6 (2016) 28558, https://doi.org/10.1038/srep28558.

[32] J. Lee, J.H. Seo, C. Nguyen-Huy, E. Yang, J.G. Lee, H. Lee, E.J. Jang, J.H. Kwak, J. H. Lee, H. Lee, K. An, Cu2O(100) surface as an active site for catalytic furfural hydrogenation, Appl. Catal. B: Environ. 282 (2021), 119576, https://doi.org/10.1016/j.apcatb.2020.119576.

[33] J. Wu, C. Liu, Y. Zhu, X. Song, C. Wen, X. Zhang, C. Wang, L. Ma, Understanding the geometric and electronic factors of PtNi bimetallic surfaces for efficient and selective catalytic hydrogenation of biomass-derived oxygenates, J. Energy Chem. 60 (2021) 16–24, https://doi.org/10.1016/j.jechem.2020.12.011.

[34] J. Yu, Y. Yang, L. Chen, Z. Li, W. Liu, E. Xu, Y. Zhang, S. Hong, X. Zhang, M. Wei, NiBi intermetallic compounds catalyst toward selective hydrogenation of unsaturated aldehydes, Appl. Catal. B: Environ. 277 (2020) 119273, https://doi.org/10.1016/j.apcatb.2020.119273.

[35] T. Xiao, P. Yan, K. Li, C. Yang, H. Yu, J. Wang, H. Yin, S. Zhou, Hollow mesoporous nanoreactors with encaged PtSn alloy nanoparticles for selective hydrogenation of furfural to furfuryl alcohol, Ind. Eng. Chem. Res. 60 (2021) 6078–6088, https://doi.org/10.1021/acs.iecr.1c00293.

[36] M.J. Taylor, L.J. Durndell, M.A. Isaacs, C.M.A. Parlett, K. Wilson, A.F. Lee, G. Kyriakou, Highly selective hydrogenation of furfural over supported Pt nanoparticles under mild conditions, Appl. Catal. B: Environ. 180 (2016) 580–585, https://doi.org/10.1016/j.apcatb.2015.07.006.

[37] Y. Shao, X. Hu, Z. Zhang, K. Sun, G. Gao, T. Wei, S. Zhang, S. Hu, J. Xiang, Y. Wang, Direct conversion of furfural to levulinic acid/ester in dimethoxymethane: Understanding the mechanism for polymerization, Green. Energy Environ. 4 (2019) 400–413, https://doi.org/10.1016/j.gee.2018.10.002.

[38] S.M. Rogers, C.R.A. Catlow, C.E. Chan-Thaw, A. Chutia, N. Jian, R.E. Palmer, M. Perdjon, A. Thetford, N. Dimitratos, A. Villa, P.P. Wells, Tandem site- and size-controlled Pd nanoparticles for the directed hydrogenation of furfural, ACS Catal. 7 (2017) 2266–2274, https://doi.org/10.1021/acscatal.6b03190.

[39] Z. Zhao, R. Bababrik, W. Xue, Y. Li, N.M. Briggs, D.-T. Nguyen, U. Nguyen, S. P. Crossley, S. Wang, B. Wang, D.E. Resasco, Solvent-mediated charge separation drives alternative hydrogenation path of furanics in liquid water, Nat. Catal. 2 (2019) 431–436, https://doi.org/10.1038/s41929-019-0257-z.

[40] G. Gao, Z. Jiang, C. Hu, Selective hydrogenation of the carbonyls in furfural and 5-hydroxymethylfurfural catalyzed by PtNi alloy supported on SBA-15 in aqueous solution under mild conditions, Front. Chem. 9 (2021), 759512, https://doi.org/10.3389/fchem.2021.759512.

[41] J. Feng, Y. He, Y. Liu, Y. Du, D. Li, Supported catalysts based on layered double hydroxides for catalytic oxidation and hydrogenation: general functionality and promising application prospects, Chem. Soc. Rev. 44 (2015) 5291–5319, https://doi.org/10.1039/c5cs00268k.

[42] Y. Yang, Z. Ren, S. Zhou, M. Wei, Perspectives on multifunctional catalysts derived from layered double hydroxides toward upgrading reactions of biomass resources, ACS Catal. 11 (2021) 6440–6454, https://doi.org/10.1021/acscatal.1c00699.

[43] Y. Zhu, W. Zhao, J. Zhang, Z. An, X. Ma, Z. Zhang, Y. Jiang, L. Zheng, X. Shu, H. Song, X. Xiang, J. He, Selective activation of C–OH, C–O–C, or C=C in furfuryl alcohol by engineered Pt sites supported on layered double oxides, ACS Catal. 10 (2020) 8032–8041, https://doi.org/10.1021/acscatal.0c01276.

[44] D. Wang, F. Ammari, R. Touroude, D.S. Su, R. Schlögl, Promotion effect in Pt–ZnO catalysts for selective hydrogenation of crotonaldehyde to crotyl alcohol: a structural investigation, Catal. Today 147 (2009) 224–230, https://doi.org/10.1016/j.cattod.2008.10.018.

[45] Y. Zhou, X. Liu, P. Yu, C. Hu, Temperature-tuned selectivity to alkanes or alcohol from ethyl palmitate deoxygenation over zirconia-supported cobalt catalyst, Fuel 278 (2020), 118295, https://doi.org/10.1016/j.fuel.2020.118295.

[46] S. Yurdakal, C. Garlisi, L. Özcan, M. Bellardita, G. Palmisano, Chapter 4 - (Photo) catalyst characterization techniques: adsorption isotherms and BET, SEM, FTIR, UV–Vis, photoluminescence, and electrochemical characterizations, in: G. Marcì, L. Palmisano (Eds.), Heterogeneous Photocatalysis, Elsevier, 2019, pp. 87–152, https://doi.org/10.1016/B978-0-444-64015-4.00004-3.

[47] D. Kwon, J.Y. Kang, S. An, I. Yang, J.C. Jung, Tuning the base properties of Mg–Al hydrotalcite catalysts using their memory effect, J. Energy Chem. 46 (2020) 229–236, https://doi.org/10.1016/j.jechem.2019.11.013.

[48] Z.M. Ni, S.J. Xia, L.G. Wang, F.F. Xing, G.X. Pan, Treatment of methyl orange by calcined layered double hydroxides in aqueous solution: adsorption property and kinetic studies, J. Colloid Interface Sci. 316 (2007) 284–291, https://doi.org/10.1016/j.jcis.2007.07.045.

[49] Z. Ren, Y. Yang, S. Wang, X. Li, H. Feng, L. Wang, Y. Li, X. Zhang, M. Wei, Pt atomic clusters catalysts with local charge transfer towards selective oxidation of furfural, Appl. Catal. B: Environ. 295 (2021) 120290, https://doi.org/10.1016/j.apcatb.2021.120290.

[50] Z. Yu, X. Lu, X. Wang, J. Xiong, X. Li, R. Zhang, N. Ji, Metal-catalyzed hydrogenation of biomass-derived furfural: particle size effects and regulation strategies, ChemSusChem 13 (2020) 5185–5198, https://doi.org/10.1002/cssc.202001467.

[51] Z. Jiang, Y.H. Zhao, L.Z. Kong, Z.Y. Liu, Y. Zhu, Y.H. Sun, Structure-dependent selective hydrogenation of alpha,beta-unsaturated aldehydes over platinum nanocrystals decorated with nickel, ChemPlusChem 79 (2014) 1258–1262, https://doi.org/10.1002/cplu.201402109.